Chemical Engineering Journal 469 (2023) 143876

Contents lists available at ScienceDirect

Chemical Engineering Journal

journal homepage: www.elsevier.com/locate/cej

Self-shedding of multifunctional biomolecular nanocarriers for H-FABP monitoring in magnetic separation self-powered photoelectrochemical and colorimetric immunoassay platform

Dongquan Leng [a], Rui Xu [a], Xiang Ren [a], Hongmin Ma [a], Lei Liu [a,*], Qin Wei [a,b,*], Huangxian Ju [a,c]

[a] Collaborative Innovation Center for Green Chemical Manufacturing and Accurate Detection, Key Laboratory of Interfacial Reaction & Sensing Analysis in Universities of Shandong, School of Chemistry and Chemical Engineering, University of Jinan, Jinan 250022, PR China
[b] Department of Chemistry, Sungkyunkwan University, Suwon 16419, Republic of Korea
[c] State Key Laboratory of Analytical Chemistry for Life Science, Department of Chemistry, Nanjing University, Nanjing 210023, PR China

ARTICLE INFO

Keywords:
Photoelectrochemical
Colorimetric immunoassay
Cu_2ZnSnS_4
Self-shedding strategy
Nano-enzyme

ABSTRACT

To embrace the challenge of the limitations of traditional nano-solid materials, biomolecular layer-by-layer assembly and single detection mode, this work innovated a dual-mode immunoassay of split-type self-powered photoelectrochemical (PEC) and colorimetric detection based on self-shedding of biomolecular nanocarriers for physiological monitoring. The self-shedding process completed in 96 microplate is that the outer MnO_2 of MnO_2-coated Fe_3O_4@Carbon nanosphere complex (Fe_3O_4@Carbon@MnO_2) is consumed by quantitative ascorbic acid. Fe_3O_4@Carbon as a peroxide-mimicking enzyme remaining with completely bare surface provides sufficient active sites and the seed solution affecting the photoanode are separated by magnetic forces. In this process, biometrics and dual-mode signal detection realize spatial isolation in mutual influence, and the sensitivity of immunoassay was further improved. The photoanode ITO/$BiVO_4$ was constructed by electrodeposition with the ad-vantages of high specific surface area and uniformity, and the hole consuming agent FeOOH was generated on electrode surface, which affects the signal of the PEC substrate to indirectly reflect the concentration of biomolecules. In addition, the self-powered biosensor constructed by assembling Cu_2ZnSnS_4 (CZTS) with excellent interface-to-volume ratio on FTO using template method as working electrode. As a proof of principle, heart fatty acid binding protein (H-FABP) was analyzed and the obtained linear range of the dual mode biosensor was from 0.050 pg/mL to 100 ng/mL with a detection limit of 0.013 pg/mL (S/N = 3).

1. Introduction

Photoelectrochemical (PEC) as a technique for converting light energy into electricity has received extensive attention owing to its merits of the controllable excitation light source, easy miniaturization of the detection device, high sensitivity and multimodal assay method [1–8]. To date, photoelectrochemical sensor detection model presents the diversification trend, in general, the traditional detection strategy is through the space steric effect of protein molecules, competition of photo between the carrier material of labeled antibody and the substrate material or enzyme catalytic activity to indirect target analyte concentration [9–14]. The assembly of PEC materials on electrodes with various biological protein molecules is a common feature of the layered modification strategies involved above [15–20], which can simplify the analytical equipment to some extent, however, the complicated operation process and the interaction between photoelectrochemical conversion and biomolecular activity hinder the improvement of immunoassay sensitivity. Therefore, it is urgent to develop a simple and efficient novel signal switch for the rapid detection of markers of disease.

Split-type PEC immunosensor based on considering the independent but mutually reflected processes of energy conversion and immunoassay can improve the performance of biological molecules detection [21–24]. However, the route to contact these two separate processes is the critical factor to improving sensor performance [25,26]. Tang et al. efficiently detected prostate-specific antigen (PSA) by adjusting surface redox reaction process and the band-edge position based on the alkalinity of electrolyte [27]. Wu et al. developed an innovative strategy for photo

* Corresponding authors at: Collaborative Innovation Center for Green Chemical Manufacturing and Accurate Detection, Key Laboratory of Interfacial Reaction & Sensing Analysis in Universities of Shandong, School of Chemistry and Chemical Engineering, University of Jinan, Jinan 250022, PR China (Q. Wei).
E-mail addresses: liulei70919@126.com (L. Liu), sdjndxwq@163.com (Q. Wei).

https://doi.org/10.1016/j.cej.2023.143876
Received 6 April 2023; Received in revised form 28 May 2023; Accepted 29 May 2023
Available online 3 June 2023

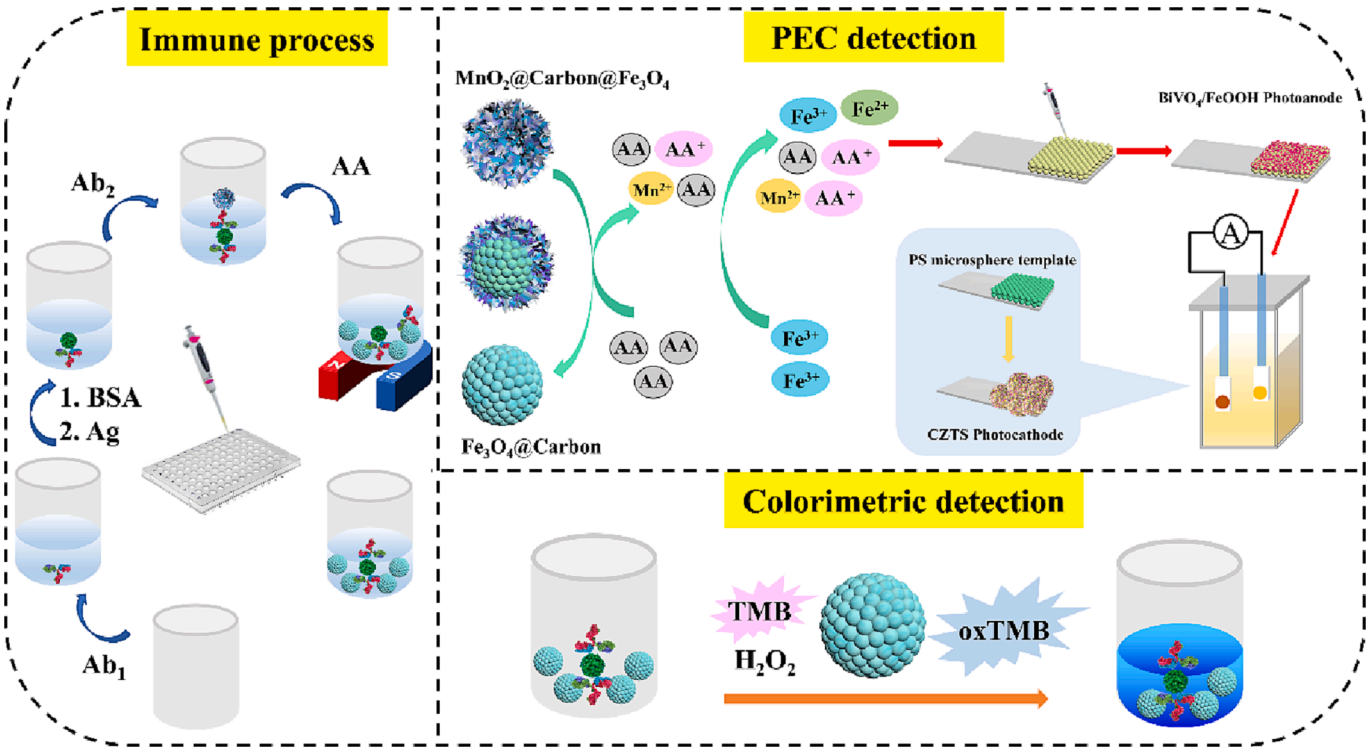

Scheme 1. Fabrication Process of Photoelectrochemical and Colorimetric Immunosensor.

deposition of silver nanoparticles on the working electrode surface by acid-interpreted silver ions for microRNA-155 detection [28]. Li et al. innovated a cationic exchange reaction between cations released in a 96-microwell plate and PEC substrate material for neuron specific enolase sensitive detection [29]. In this work, a novel split-type strategy of generating solid hole absorbent on the surface of photoanode in situ was optimized and applied to the self-powered photosensor, and colorimetric analysis was used to further improve the accuracy of immunoassay. In addition, compared with the traditional single-mode biosensor, dual-mode biosensor could obtain more accurate and comprehensive information [30]. The dual-mode biosensor can improve the reliability and stability of the sensor and overcome the problem that the single signal sensor is prone to environmental interference [31]. Moreover, dual-mode sensors can also realize dual redundancy design, increasing the reliability and stability of sensors, even if one sensor fails, the other can continue to work [32]. Colorimetric analysis has the advantages of low cost, convenience and portability [33]. In this work, colorimetric analysis and PEC analysis are combined, which would be of great significance for diagnosing and monitoring diseases.

Bismuth vanadate ($BiVO_4$) is a high-performance n-type semiconductor widely applied in the field of photocatalysis and photoelectrochemical due to its proper valence band and conduction band position, narrow band gap (~2.4 eV) and extremely stable properties [34–36], which is an indispensable basic material in the application of PEC immunoassay in clinical detection process. So far, the heterojunction structure ($BiVO_4/ZnIn_2S_4$, $BiVO_4$/FeOOH, Mo:$BiVO_4$, $BiVO_4/CoMoO_4$) based on bismuth vanadate has been extensively expanded [37,38]. Among them, the $BiVO_4$/FeOOH has a good performance of generating photocurrent by excitation of visible light without any hole sacrificial agent. And it was surprising to find that FeOOH films could be naturally generated on $BiVO_4$ at room temperature [39–41]. In addition, FeOOH as a p-type cocatalysts could improve the absorption efficiency of visible light effectively and store photogenerated holes from the $BiVO_4$ bulk for suppressing electron-hole recombination [42]. Cu_2ZnSnS_4 (CZTS) has attracted extensive attention in the field of photocatalysis and photocells due to its advantages of efficient visible light absorption, narrow band gap, abundant elements and environmental friendliness [43]. However, few scholars have paid attention to the high-performance material in the field of photoelectrochemical immunoassay. In this work, porous CZTS synthesized by template method as photocathode was applied for immunoassay for the first time.

To embrace the challenge of the limitations of traditional nano-solid materials, biomolecular layer-by-layer assembly and single detection mode, this work innovated a dual-mode immunoassay of split-type self-powered photoelectrochemical (PEC) and colorimetric detection based on self-shedding of biomolecular nanocarriers for biological molecules detection. The photoanode ITO/$BiVO_4$ was constructed by electrodeposition with the advantages of high specific surface area and uniformity, and the hole consuming agent FeOOH was generated on electrode surface, which affects the signal of the PEC substrate to indirectly reflect the concentration of biomolecules. In addition, the self-powered biosensor constructed by assembling Cu_2ZnSnS_4 (CZTS) with excellent interface-to-volume ratio on FTO using template method as working electrode. The self-shedding process completed in the microplate is that the outer MnO_2 of MnO_2-coated Fe_3O_4@Carbon nanosphere complex (Fe_3O_4@Carbon@MnO_2) is consumed by quantitative Ascorbic acid (AA). The remaining AA in the microplate influence a solution containing ferric iron ions to form FeOOH on the ITO/$BiVO_4$ electrode surface. More importantly, Fe_3O_4@Carbon remaining in the microplate with completely bare surface provides sufficient active sites for catalyzing TMB as a peroxide-mimicking enzyme, thus further improving the sensitivity of the colorimetric immunoassay.

2. Experimental section

2.1. Reagents and equipment

The experimental details (equipment, reagents, etc.) were placed in *Supporting Information*.

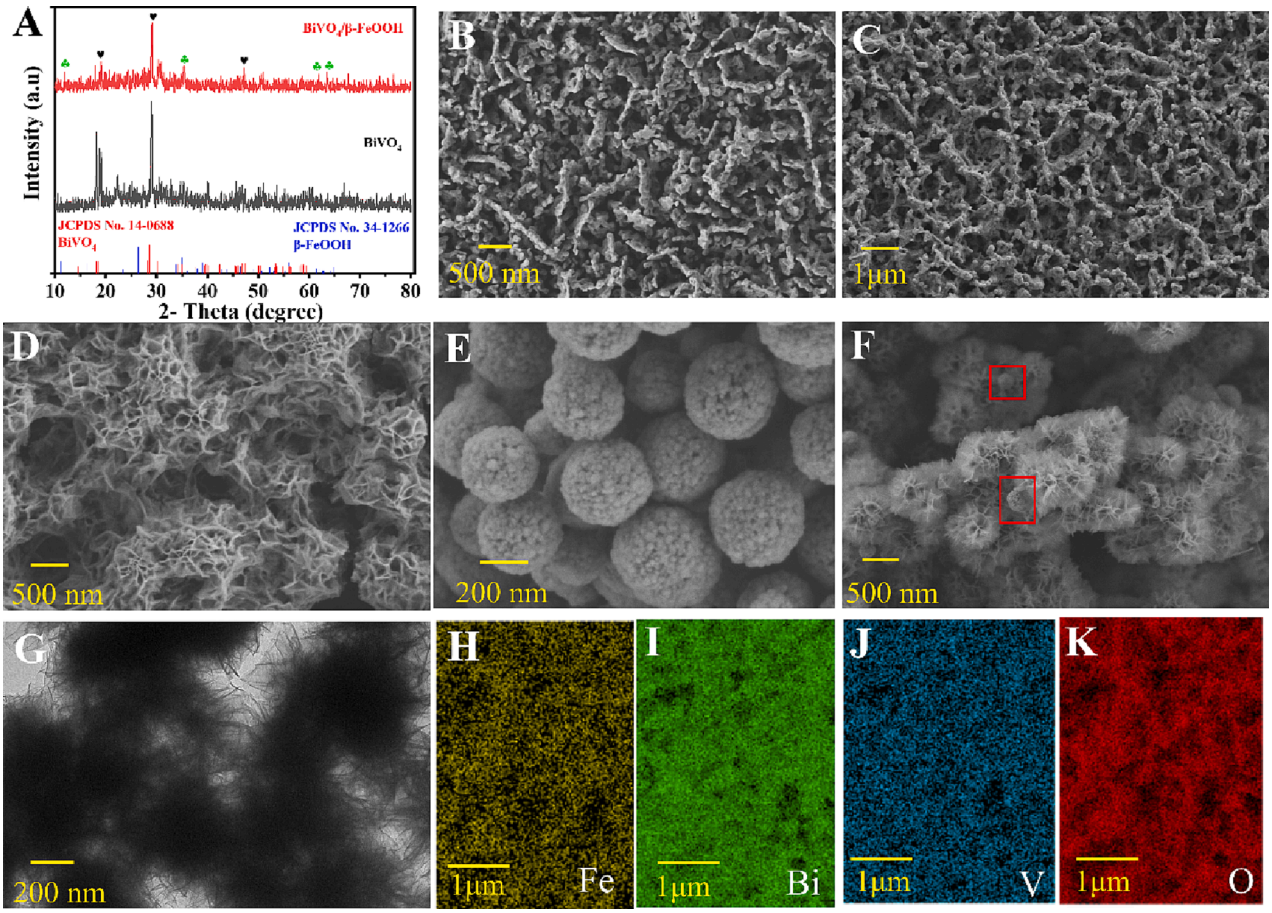

Fig. 1. (A) XRD image of $BiVO_4$ and $BiVO_4$/FeOOH, (B) SEM image of $BiVO_4$, (C) SEM image of $BiVO_4$/FeOOH, (D) SEM image of Cu_2ZnSnS_4, (E) SEM image of Fe_3O_4, and (F) and (G)SEM and TEM images of Fe_3O_4@Carbon@MnO_2, (H), (I), (J) and (K) mapping images of Fe, Bi, V and O elements.

2.2. Preparation of Cu_2ZnSnS_4

Cu_2ZnSnS_4 was prepared according to the previously reported template method [43]. Preparation of polystyrene (PS) spheres: In a three-necked flask, 20 mL of styrene monomer, 1 mL of methylacrylic acid and 100 mL of deionized water were added. The above uniformly mixed solution was heated to 115℃ and refluxed for 20 min. Then 10 mL of solution containing 0.25 g of potassium persulfate was added with continue stirring for 120 min. The polystyrene spheres after centrifugation and washing were stored in the solution ($V_{ethanol}$: $V_{ultrapure\ water}$ = 2:1). The desired coverage area of FTO was immersed in the above solution for 10 min, and then the FTO was lifted at a slow speed to ensure uniform coverage of the polystyrene spheres. The FTO/PS was dried at 60℃ on a heating plate before calcining at 90℃ for 1 h in a muffle furnace.

Preparation of CZTS: Firstly, 4 mmol of $ZnCl_2$, 3 mmol of $CuCl_2{\cdot}2H_2O$, 3 mmol of $SnCl_2{\cdot}2H_2O$ and 0.02 mol of thiourea was added to 20 mL of methanol solution with stirring for 3 h. After that, the prepared FTO/PS was immersed in the above solution for 10 s, and then dried on a heating plate at 60℃. Finally, it was transferred to a muffle furnace for calcination at 350℃ for 1 h with a heating rate of 5 ℃/min.

2.3. Preparation of Fe_3O_4@Carbon@MnO_2 core–shell microspheres

0.2 g Fe_3O_4 was dispersed in 200 mL of tris(hydroxymethyl) aminomethane buffer (pH = 8.5) by ultrasound, and then dopamine hydrochloride was added and stirred for 12 h under mechanical stirring. After that, the reaction mixture was magnetically separated and washed for 2 times with absolute ethanol, then obtained product was placed in a tube furnace and heated at 500℃ for 4 h under nitrogen gas with a heating rate of 2 ℃/min. The prepared material above was dispersed in a solution containing 0.64 g potassium permanganate, mechanically stirred for 0.5 h, and then heated at 170℃ for 10 h. Finally, the reaction product was magnetically washed several times and dried overnight in a vacuum environment to obtain Fe_3O_4@Carbon@MnO_2 core–shell microspheres.

2.4. Preparation of Fe_3O_4@Carbon@MnO_2-Ab_2

20 mg of Fe_3O_4@Carbon@MnO_2 was evenly dispersed in 10 mL of absolute ethanol containing 0.15 mL of APTES, and then the above mixture was heated for 1.5 h at 70℃ with magnetic stirring. After several magnetic washing, 600 μL of glutaraldehyde and 360 μL of ultrapure water were added and shaken for 4 h. Then 1 mL Ab_2 was added, and the mixture was separated by magnetic force after shaking for 2 h at room temperature. Finally, the secondary antibody complex was dispersed in PBS solution and placed in a 4℃ refrigerator for later use.

2.5. Fabrication and detection procedure of the immunosensor

As illustrated in Scheme 1, First, Ab_1 was incubated overnight in a 96-microwell plate, and then BSA, Ag, and Fe_3O_4@Carbon@MnO_2-Ab_2 were incubated sequentially for 1 h each time at room temperature. Before proceeding to the next step, the solution of the last hatching was transferred and the microwells were washed by PBS (pH = 7.4). After that, 10 μL of PBS solution containing 25 mM ascorbic acid was added. After 10 min, the solution was separated from Fe_3O_4 in the microplate under the action of magnetic force, and then the removed solution and

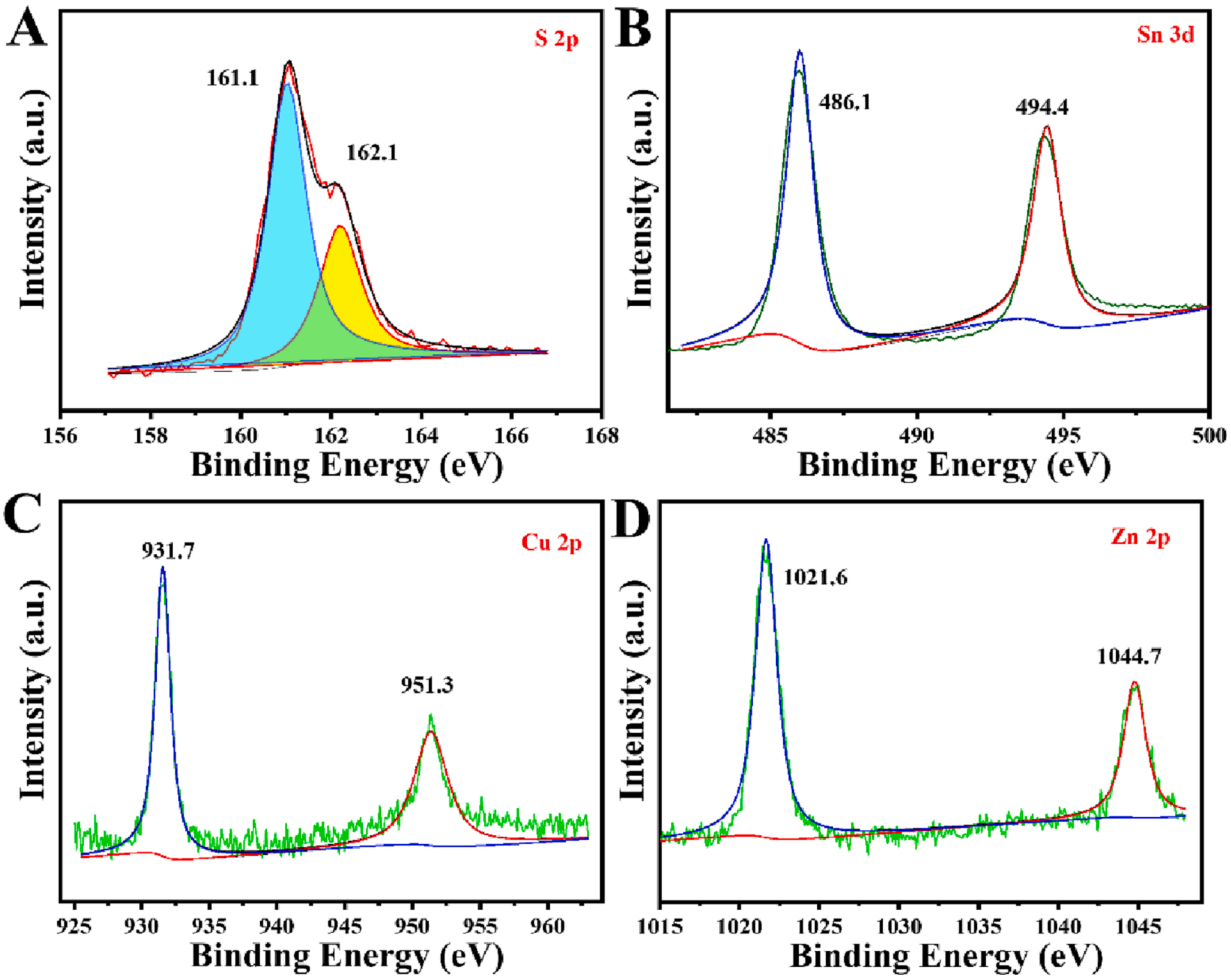

Fig. 2. (A) XPS spectra of S 2p (B) XPS spectra of Sn 3d, (C) XPS spectra of Cu 2p, (D) XPS spectra of Zn 2p.

10 μL the solution containing Fe^{3+} were dropped on the ITO/$BiVO_4$ electrode in anaerobic environment. After 30 min, the electrode surface was fully cleaned with ultrapure water. Photoanode was used as reference/counter electrode, photocathode as working electrode, and PBS as electrolyte solution for photocurrent test. Meanwhile, 50 μL TMB and 10 μL H_2O_2 were added to the microplates, and colorimetric detection were performed 20 min later.

3. Results and discussion

3.1. Characterization of materials $BiVO_4$/FeOOH, Cu_2ZnSnS_4, Fe_3O_4@Carbon@MnO_2

The X-ray diffraction (XRD), Scanning electron microscopy (SEM), transmission electron microscopy (TEM) physical characterization technologies were applied to characterize the composition and microstructure of $BiVO_4$/FeOOH, Cu_2ZnSnS_4, Fe_3O_4@Carbon@MnO_2. In Fig. 1A, XRD patterns of $BiVO_4$ are shown, the diffraction peaks of $BiVO_4$ at 18.669° (110), 18.988° (011), 28.586° (−130), 28.822° (−121), 28.947° (121), 49.960° (−202) matched with the reference (JCPDS, PDF #14–0688), and the diffraction peaks of β-FeOOH (JCPDS, PDF #34–1266) at 11.842 (110), 35.161 (211), 61.642 (611) perfectly matched with the characteristic peaks of the XRD pattern of the generated $BiVO_4$/FeOOH, indicating the well-crystallized nanostructure of FeOOH. In addition, the XRD pattern shown in Figure S1 proves the successful synthesis of Fe_3O_4@Carbon@MnO_2. SEM images of $BiVO_4$ and $BiVO_4$/FeOOH are presented in Fig. 1B, C to investigate the morphology information. Compared with disordered-fence $BiVO_4$

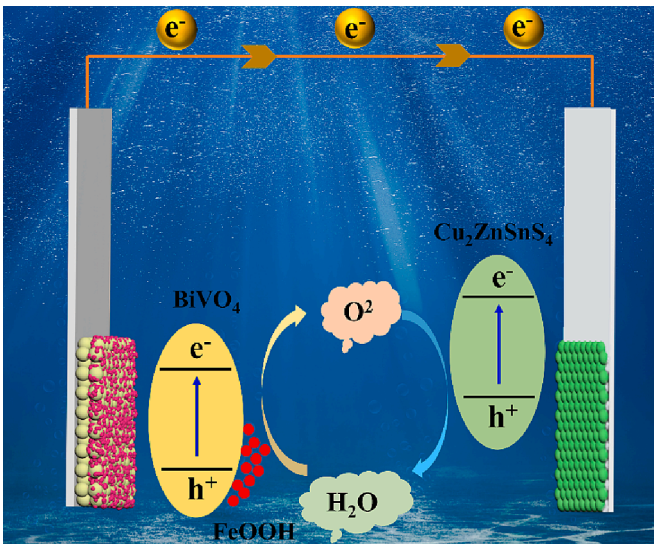

Fig. 3. Mechanism of pec.

(Fig. 1B), it is obvious that $BiVO_4$/FeOOH (Fig. 1C) is covered with a thin film, and the existence of Fe, Bi, V, and O elements are demonstrated by corresponding mapping simultaneously in Fig. 1H, J, K, L and S2. It is also profit from the loose surface structure of $BiVO_4$ that FeOOH film could be quickly and evenly attached to its surface. The porous

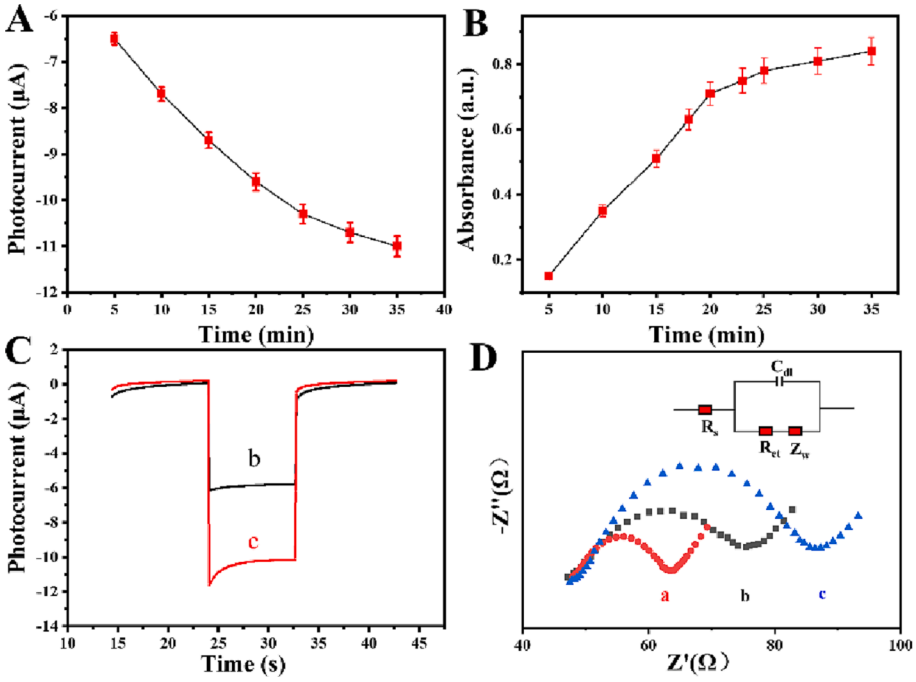

Fig. 4. (A) The time of FeOOH generation, (B) The time of colorimetric detection, (C) PEC signal and (D) EIS of (a) ITO, (b) ITO/$BiVO_4$, (c) ITO/$BiVO_4$/FeOOH.

morphology of Cu_2ZnSnS_4 in Fig. 1D and sufficient contact with electrolyte solution provide sufficient prerequisite for electron transfer. And corresponding mapping is shown in Figure S3, the homogeneous dispersion of Cu, Zn, Sn and S further proves the successful doping of various elements in porous materials synthesized of Cu_2ZnSnS_4 by template method. As can be seen in Fig. 1E, the Fe_3O_4 nanosphere exhibits the characteristics of uniform size and dispersion, which provides a good basic carrier for the in-situ growth of polydopamine film and MnO_2 nanosheet on its surface. Fig. 1F ang G indicate the core–shell structure of Fe_3O_4@Carbon@MnO_2, it is obvious that MnO_2 nanosheets polymerize on the surface of Fe_3O_4@Carbon to form a nanoflower structure.

As shown in Figure S4 and Fig. 2, Cu_2ZnSnS_4 was further confirmed by the X-ray photoelectron spectra (XPS) analyses. The S 2p core level spectra of Cu_2ZnSnS_4 shown in Fig. 3A represented the peak position of S $2p_{1/2}$ and S $2p_{3/2}$ at 162.1 and 161.1 eV that is consistent with S^{2-}. The Sn 3d peaks were located at 486.1 and 494.4 eV matched well with Sn $3d_{5/2}$ and Sn $3d_{3/2}$ orbitals of Sn^{4+} state. The two deconvoluted peaks at 931.7 eV (Cu $2p_{3/2}$) and 951.3 eV (Cu $2p_{1/2}$) as shown in Fig. 2C, the + 1 valence of Cu element was confirmed by the binding energy between Cu $2p_{3/2}$ and Cu $2p_{1/2}$ is about 19.6 eV. In Fig. 2D, 1044.7 eV and 1021.6 eV of Zn $2p_{1/2}$ and Zn $2p_{3/2}$ corresponded to binding energies of Zn 2p peaks, and divalent Zn^{2+} was proved in Cu_2ZnSnS_4.

3.2. Formation of FeOOH and possible mechanisms of PEC and colorimetric detection

Ascorbic acid containing the enediol group reacts with the amphoteric oxide MnO_2 to form dehydroascorbic acid (DHA). The remaining ascorbic acid will further reduce the ferric (Fe^{3+}) to divalent iron ions (Fe^{2+}). In the solution rich in chloride anions, Fe^{3+} hydrolyzed and accumulated into β-FeOOH on the surface of $BiVO_4$ with a large specific surface area, while Fe^{2+} cannot directly generate FeOOH under anaerobic environment. The process of β-FeOOH nanofilm formation can be simply understood as the hydrolysis of $FeCl_3$, and the deprotonation of the hydrated ferric ion first formed in the solution to form a monomer tightly bound to the hydroxide ligand. Then, the Cl^- centered tunnel structure is formed by arranging the polymeric chains in a body-centered filling pattern, which would stabilize the framework to form β-FeOOH. The decomposition of manganese dioxide on the surface of the material makes the catalytic active site of Fe_3O_4@Carbon completely exposed to the solution, which provides a more convenient channel for the rapid oxidation of 3,3′,5,5′-tetramethylbenzidine (TMB) to generate blue oxTMB.

The possibility of photogenerated carrier transmission and photoelectrical signal enhancement in self-powered photoelectrochemical consisting of photoanode and photocathode were illustrated in Fig. 3. Owing to the ultrathin β-FeOOH with rich oxygen vacancies directly growing on the nanoporous $BiVO_4$, the interconnected framework structure formed provides a convenient and fast channel for carrier transport. The electrons inside $BiVO_4$ are excited by photons, leading to the separation of charge carriers, and the photogenerated holes in the valence band position are transferred to the ultrathin β-FeOOH layer. The ultrathin structure and abundant oxygen vacancies of β-FeOOH provide prerequisites for hole trapping and migration. Because of the above reasons, these holes concentrated on the surface of the photoanode are easier to carry out oxygen evolution reaction (OER), at the same time, the photogenerated electrons transferred to the conduction band position by photoexcitation on the surface of the photocathode undergo oxygen reduction reaction (ORR). The above reasons facilitate to achieve self-powered sensors without additional electron donors and acceptors while facilitating the separation of electrons and holes.

3.3. Feasibility analysis of immunosensor

A photocurrent response test was performed to verify the rate at which the solution containing ferric iron ions hydrolyzed with different retention times (5, 10, 15, 20, 25, 30, 35 min) on the electrode surface to produce FeOOH, the concentration of target substance was 0.05 ng/mL. As shown in Fig. 4A, it can be clearly proved that the photocurrent response becomes stronger with the prolongation of time, which reflects that the degree of ferric ion hydrolysis is proportional to time. However, it can be seen that the hydrolyzed rate changed slightly slowly after 25 min. Considering the time cost of detecting samples, 25 min was determined as the best reaction time for hydrolysis time. In addition, the color display efficiency of TMB catalyzed by peroxidase nano enzyme

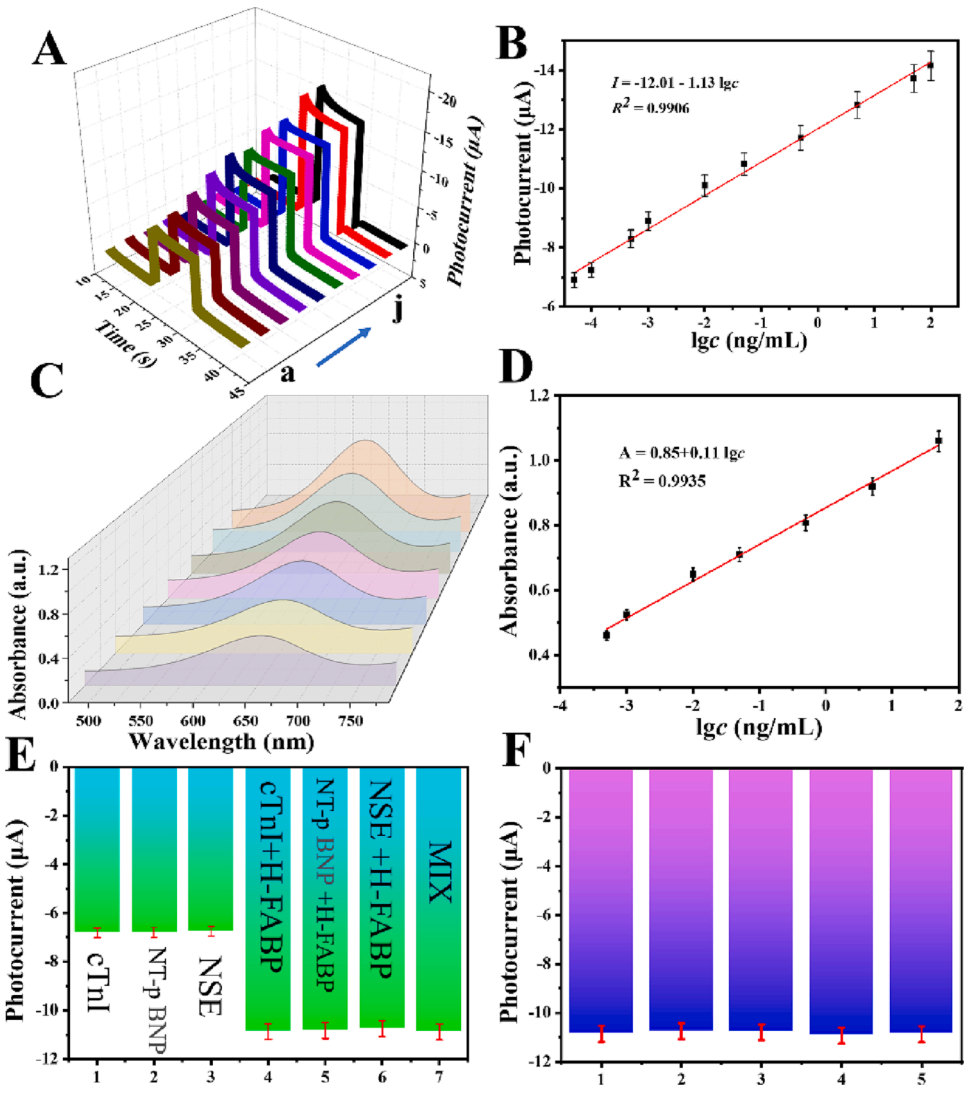

Fig. 5. (A) Photocurrent response and (B) the corresponding calibration curve of H-FABP detection: (a-j): 0.00005, 0.0001, 0.0005, 0.001, 0.01, 0.05, 0.5, 5, 50, 100 ng/mL, (C) Absorption spectra (D) the corresponding calibration curve at 0.0005, 0.001, 0.01, 0.05, 0.5, 5, 50 ng/mL (E) the test of selectivity. (c = 0.05 ng/mL), (F) The test of reproducibility (c = 0.05 ng/mL). Error bars = SD (n = 3).

(Fe_3O_4@Carbon) under the action of hydrogen peroxide was also tested, and the concentration of target substance was 0.05 ng/mL. Up to 20 min, the absorption of UV visible light increased rapidly, but the rate slowed down significantly after that (Fig. 4B). Therefore, 20 min was chosen as the colorimetric detection time.

Not only the physical characterization, but also the electrochemical characterization techniques were used to further prove the feasibility of the sensor. In the Fig. 4C, it can be seen that only the photocurrent response of $BiVO_4$ by electrodeposition and in situ growth is weaker than that of FeOOH as a hole absorber attached to the surface of the photoelectric anode. Moreover, the electrochemical impedance of naked ITO, ITO/$BiVO_4$ and ITO/$BiVO_4$/FeOOH were measured in the $K_3[Fe(CN)_6]/K_4[Fe(CN)_6]$ solution (Fig. 4D). The above results proved that the working electrode and counter electrode of the sensor were successfully prepared.

3.4. H-FABP analysis

H-FABP as a novel small cytosolic protein abundant can be regarded as a biomarker with high sensitivity and specificity for the detection of myocardial infarction. The target antigen H-FABP was selected to further investigate the sensing performance based on the advances of the proposed biosensing system and the PEC technique. Based on optimized experimental conditions, analytical performances of the biosensor for standard target antigen H-FABP detection in Fig. 5A from 0.05 pg/mL to 100 ng/mL was further explored. And by plotting PEC signal response the logarithm of H-FABP concentration, a calibration curve (Fig. 5B) I = -12.01–1.13 lg$c$ (ng/mL), (R^2 = 0.9906) was correspondingly obtained with the limit of detection (LOD, 0.013 pg/mL) of the biosensor. At the same time, colorimetric analysis (Fig. 5C) was carried out in a 96-microwell plate, and the calibration curve can be obtained by analyzing the data obtained from the detection of different concentrations of the target in the range of 0.0005–50 ng/mL, the equation (Fig. 5D) was A = 0.85 + 1.1 lg$c$ (ng/mL), R^2 = 0.9935. The LOD was calculated to be 0.16 pg/mL (S/N = 3). By comparing the sensor mentioned in this work with the reported method in photoelectric and colorimetric detection, it can be seen that this work has considerable advantages in detection range and detection limit (Table S1 and S2).

3.5. Analysis of the immunosensor performance

The specificity, stability and repeatability of biosensors are important conditions for clinical detection. In order to verify the specificity of target analyte detection, cTnI, NT-pro BNP and NSE were selected as

interfering substances. As can be seen in the Fig. 5E, when interfering substances were detected alone, the photocurrent signal response was consistent with that of bare electrodes attached only to the base material. The above substances were added to the solution containing the target, and relative standard deviation (RSD) of the results was found to be between 2.8% and 4.3%, which proved good specificity of the biosensor. Through the detection of antigen concentration of 0.05 ng/mL, the current response of the prepared electrode did not weaken significantly after 10 cycles of testing, which proved that the sensor has good stability. In addition, the prepared electrodes were tested five times under the same conditions with a concentration of 0.05 ng/mL antigen, the corresponding RSD is 4.2%, which indicates that the sensor has good repeatability.

3.6. Serum sample analysis

In pretreated 1:10 dilution of human serum sample, Standard addition assays were employed to evaluate the accuracy and utility of the proposed biosensor by adding different concentrations of the target antigen H-FABP. In the results shown in Table S3, the acceptable and reasonable recoveries range of 96.6% − 104.9% with RSD values of 2.8% − 4.2% were obtained when different concentrations of H-FABP were added. The above data results indicate that the proposed sensing strategy has great application potential in clinical diagnosis.

4. Conclusion

In summary, a dual-mode immunoassay of split-type self-powered photoelectrochemical (PEC) and colorimetric detection based on self-shedding of biomolecular nanocarriers for pathological examinations and physiological monitoring was reported. Secondary antibody marker (Fe_3O_4@Carbon@MnO_2) can not only be used as the initial material affecting the photocurrent signal, but also can be used for colorimetric detection as peroxidase mimic enzyme after shedding. Fe_3O_4@Carbon remaining in the microplate with completely bare surface provides sufficient active sites for catalyzing TMB as a peroxide-mimicking enzyme, thus further improving the sensitivity of the colorimetric immunoassay. The photoanode ITO/$BiVO_4$ was constructed by electrodeposition with the advantages of high specific surface area and uniformity, in addition, the self-powered biosensor constructed by assembling Cu_2ZnSnS_4 (CZTS) with excellent interface-to-volume ratio on FTO using template method as working electrode. The biosensors constructed in this work would add an unexpected perspective to the field of photoelectric analysis and colorimetric analysis.

Declaration of Competing Interest

The authors declare that they have no known competing financial interests or personal relationships that could have appeared to influence the work reported in this paper.

Data availability

The authors do not have permission to share data.

Acknowledgements

This study was supported by the National Natural Science Foundation of China (No.22274062, 22206056), the Shandong Provincial Natural Science Foundation (No. ZR2020QB093), Special Foun dation for Taishan Scholar Professorship of Shandong Province.Jinan Scientific Research Leader Workshop Project (2019GXRC027), and Special Foundation for Taishan Scholar Professorship of Shandong Province.

Appendix A. Supplementary data

Supplementary data to this article can be found online at https://doi.org/10.1016/j.cej.2023.143876.

References

[1] Z. Farka, T. Jurik, D. Kovar, L. Trnkova, P. Skladal, Nanoparticle-based immunochemical biosensors and assays: recent advances and challenges, Chem. Rev. 117 (15) (2017) 9973–10042.
[2] X. Gao, Q. Cai, H. Li, G. Jie, Supersandwich nanowire/quantum dots sensitization structure-based photoelectrochemical "signal-on" platform for ultrasensitive detection of thrombin, Anal. Chem. 92 (9) (2020) 6734–6740.
[3] S. Jiaju, C. Zichao, Z. Chunqin, S. Meiqi, L. Han, Z. Shusheng, Z. Zhen, Photoelectrochemical biosensing platforms for tumor marker detection, Coord. Chem. Rev. (2022).
[4] H. Li, M. Han, X. Weng, Y. Zhang, J. Li, DNA-tetrahedral-nanostructure-based entropy-driven amplifier for high-performance photoelectrochemical biosensing, ACS Nano 15 (1) (2021) 1710–1717.
[5] M.J. Li, H.J. Wang, R. Yuan, Y.Q. Chai, A sensitive label-free photoelectrochemical aptasensor based on a novel PTB7-Th/H_2O_2 system with unexpected photoelectric performance for C-reactive protein analysis, Biosens. Bioelectron. 181 (2021), 113162.
[6] Q. Zhang, C. Wang, Y. Tian, Y. Liu, F. You, K. Wang, J. Wei, L. Long, J. Qian, Growth of AgI semiconductors on tailored 3D porous Ti_3C_2 MXene/graphene oxide aerogel to develop sensitive and selective "signal-on" photoelectrochemical sensor for H_2S determination, Anal. Chim. Acta 1245 (2023), 340845.
[7] Y. Tian, C. Wang, Q.i. Zhang, H. Cui, Y. Liu, K. Wang, J. Wei, L. Long, J. Qian, Tailored Ti_3C_2 MXene/SnS_2 nanocomposites to realize both sensitive photoelectrochemical determination and efficient photocatalytic detoxification of Cr(VI), Sensor. Actuat. B: Chem. 382 (2023) 133496.
[8] X. Liu, Y. Zhao, F. Li, Nucleic acid-functionalized metal-organic framework for ultrasensitive immobilization-free photoelectrochemical biosensing, Biosens. Bioelectron. 173 (2021), 112832.
[9] Q. Cai, D. Wu, H. Li, G. Jie, H. Zhou, Versatile photoelectrochemical and electrochemiluminescence biosensor based on 3D CdSe QDs-DNA nanonetwork-SnO_2 nanoflower coupled with DNA walker amplification for HIV detection, Biosens. Bioelectron. 191 (2021), 113455.
[10] H.M. Deng, M.J. Xiao, Y.Q. Chai, R. Yuan, Y.L. Yuan, P_3HT-PbS nanocomposites with mimicking enzyme as bi-enhancer for ultrasensitive photocathodic biosensor, Biosens. Bioelectron. 197 (2022), 113806.
[11] D. Liao, G. Liang, Y. Liu, W. Yan, Y. Guo, W. Liang, C. Dong, L. Fan, Design an efficient photoelectrochemical aptasensor for PCB72 based on CdTe@CdS core@shell quantum dots-decorated TiO_2 nanotubes, J. Hazard. Mater. 441 (2023), 129901.
[12] D. Long, Y. Tu, Y. Chai, R. Yuan, Photoelectrochemical assay based on SnO_2/BiOBr p-n heterojunction for ultrasensitive DNA detection, Anal. Chem. 93 (38) (2021) 12995–13000.
[13] Y. Qin, J. Wen, X. Wang, L. Jiao, X. Wei, H. Wang, J. Li, M. Liu, L. Zheng, L. Hu, W. Gu, C. Zhu, Iron single-atom catalysts boost photoelectrochemical detection by integrating interfacial oxygen reduction and enzyme-mimicking activity, ACS Nano 16 (2) (2022) 2997–3007.
[14] A. Victorious, S. Saha, R. Pandey, L. Soleymani, Enhancing the Sensitivity of Photoelectrochemical DNA biosensing using plasmonic DNA barcodes and differential signal readout, Angew. Chem. Int. Ed. Engl. 60 (13) (2021) 7316–7322.
[15] X. Yan, H. Li, T. Yin, G. Jie, H. Zhou, Photoelectrochemical biosensing platform based on in situ generated ultrathin covalent organic framework film and $AgInS_2$ QDs for dual target detection of HIV and CEA, Biosens. Bioelectron. 217 (2022), 114694.
[16] H. Yang, Q. Zhou, Z. Fang, W. Li, Y. Zheng, J. Ma, Z. Wang, L. Zhao, S. Liu, Y. Shen, Y. Zhang, Carbon nitride of five-membered rings with low optical bandgap for photoelectrochemical biosensing, Chem 7 (10) (2021) 2708–2721.
[17] X. Ye, X. Wang, Y. Kong, M. Dai, D. Han, Z. Liu, FRET modulated signaling: A versatile strategy to construct photoelectrochemical microsensors for in vivo analysis, Angew. Chem. Int. Ed. Engl. 60 (21) (2021) 11774–11778.
[18] S. Meng, D. Liu, Y. Li, N. Dong, S. Liu, C. Liu, X. Li, T. You, Photoelectrochemical and visual dual-mode sensor for efficient detection of Cry1Ab protein based on the proximity hybridization driven specific desorption of multifunctional probe, J. Hazard. Mater. 441 (2023), 129759.
[19] S.T. Shanmugam, S. Trashin, K. De Wael, Singlet oxygen-based photoelectrochemical detection of DNA, Biosens. Bioelectron. 195 (2022), 113652.
[20] Q. Zhou, H. Chen, K. Wang, H. Zhang, L. Pan, H. Zheng, Y. Zhou, Z. Hu, Z. Peng, J. Wan, B. Wang, Photoelectrochemical immunosensor for archaeological silk microtrace detection based on tailored monoclonal antibody and ZnO nanowires array, Sensor. Actuat. B: Chem. 374 (2023) 132804.
[21] Y.T. Gong, F. Yuan, Y. Dong, Z. Li, G.L. Wang, Switched photoelectrochemistry of carbon dots for split-type immunoassay, Anal. Chim. Acta 1014 (2018) 19–26.
[22] L. Su, Y. Song, C. Fu, D. Tang, Etching reaction-based photoelectrochemical immunoassay of aflatoxin B1 in foodstuff using cobalt oxyhydroxide nanosheets-coating cadmium sulfide nanoparticles as the signal tags, Anal. Chim. Acta 1052 (2019) 49–56.
[23] K. Zhang, S. Lv, Z. Lin, M. Li, D. Tang, Bio-bar-code-based photoelectrochemical immunoassay for sensitive detection of prostate-specific antigen using rolling circle

amplification and enzymatic biocatalytic precipitation, Biosens. Bioelectron. 101 (2018) 159–166.
[24] J. Zhuang, D. Tang, W. Lai, M. Xu, D. Tang, Target-induced nano-enzyme reactor mediated hole-trapping for high-throughput immunoassay based on a split-type photoelectrochemical detection strategy, Anal. Chem. 87 (18) (2015) 9473–9480.
[25] R. Zeng, H. Gong, Y. Li, Y. Li, W. Lin, D. Tang, D. Knopp, CRISPR-Cas12a-derived photoelectrochemical biosensor for point-of-care diagnosis of nucleic acid, Anal. Chem. 94 (20) (2022) 7442–7448.
[26] J. Shu, D. Tang, Recent advances in photoelectrochemical sensing: from engineered photoactive materials to sensing devices and detection modes, Anal. Chem. 92 (1) (2020) 363–377.
[27] Q. Lin, X. Huang, L. Lu, D. Tang, Snowflake-like CdS@$ZnIn_2S_4$ heterojunction-based photocatalyst-electrolyte effect: An innovative mode for photoelectrochemical immunoassay, Biosens. Bioelectron. 216 (2022), 114679.
[28] Y.-Y. Wei, S.-H. Wu, Q.-M. Wang, J.-J. Sun, A novel split-type photoelectrochemical biosensor based on double-strand specific nuclease-assisted cycle amplification coupled with plasmonic Ag enhanced $BiVO_4$ performance for sensitive detection of microRNA-155, Sensor. Actuat. B: Chem. 369 (2022) 132251.
[29] D. Leng, J. Zhao, X. Ren, R. Xu, L. Liu, X. Liu, Y. Li, Q. Wei, $MoSe_2$/CdSe heterojunction destruction by cation exchange for photoelectrochemical immunoassays with a controlled-release strategy, Anal. Chem. 93 (30) (2021) 10712–10718.
[30] Y. Zhou, S. Lv, X.Y. Wang, L. Kong, S. Bi, Biometric photoelectrochemical-visual multimodal biosensor based on 3D hollow HCdS@Au nanospheres coupled with target-induced ion exchange reaction for antigen detection, Anal. Chem. 94 (41) (2022) 14492–14501.
[31] J. Wei, W. Chang, A. Qileng, W. Liu, Y. Zhang, S. Rong, H. Lei, Y. Liu, Dual-modal split-type immunosensor for sensitive detection of microcystin-LR: Enzyme-induced photoelectrochemistry and colorimetry, Anal. Chem. 90 (15) (2018) 9606–9613.
[32] Y. Fu, Q. Yu, Q. Zhang, X. Zhang, C. Du, J. Chen, A photocurrent-polarity-switching biosensor for highly selective assay of mucin 1 based on target-induced hemin transfer from ZrO_2 hollow spheres to G-quadruplex nanowires, Biosens. Bioelectron. 192 (2021), 113547.
[33] D. Han, H. Yang, Z. Zhou, K. Wu, J. Ma, Y. Fang, Q. Hong, G. Xi, S. Liu, Y. Shen, Y. Zhang, Photoelectron storages in functionalized carbon nitrides for colorimetric sensing of oxygen, ACS sens. 7 (8) (2022) 2328–2337.
[34] J. Du, X. Zhong, H. He, J. Huang, M. Yang, G. Ke, J. Wang, Y. Zhou, F. Dong, Q. Ren, L. Bian, Enhanced photoelectrochemical water oxidation performance on $BiVO_4$ by coupling of $CoMoO_4$ as a hole-transfer and conversion cocatalyst, ACS Appl. Mater. Interfaces 10 (49) (2018) 42207–42216.
[35] M. Rohloff, B. Anke, O. Kasian, S. Zhang, M. Lerch, C. Scheu, A. Fischer, Enhanced photoelectrochemical water oxidation performance by fluorine incorporation in $BiVO_4$ and Mo:$BiVO_4$ thin film photoanodes, ACS Appl. Mater. Interfaces 11 (18) (2019) 16430–16442.
[36] Y. Wang, D. Wang, S. Dong, J. Qiao, Z. Zeng, S. Shao, A visible-light-driven photoelectrochemical sensing platform based on the $BiVO_4$/FeOOH photoanode for dopamine detection, Electrochim. Acta 414 (2022) 140207.
[37] J. Shu, Z. Qiu, Z. Lin, G. Cai, H. Yang, D. Tang, Semiautomated support photoelectrochemical immunosensing platform for portable and high-throughput immunoassay based on Au nanocrystal decorated specific crystal facets $BiVO_4$ photoanode, Anal. Chem. 88 (24) (2016) 12539–12546.
[38] S. Lv, K. Zhang, Y. Zeng, D. Tang, Double photosystems-based 'Z-Scheme' photoelectrochemical sensing mode for ultrasensitive detection of disease biomarker accompanying three-dimensional DNA walker, Anal. Chem. 90 (11) (2018) 7086–7093.
[39] T. Kamimura, S. Nasu, T. Segi, T. Tazaki, H. Miyuki, S. Morimoto, T. Kudo, Influence of cations and anions on the formation of β-FeOOH, Corros. Sci. 47 (10) (2005) 2531–2542.
[40] C. Rémazeilles, P. Refait, On the formation of β-FeOOH (akaganéite) in chloride-containing environments, Corros. Sci. 49 (2) (2007) 844–857.
[41] X. Wei, X. Mou, Y. Zhou, Y. Li, W. Shen, Fabrication of rod-shaped β-FeOOH: the roles of polyethylene glycol and chlorine anion, Science China Chemistry 59 (7) (2016) 895–902.
[42] Q. Zhou, Y. Lin, J. Shu, K. Zhang, Z. Yu, D. Tang, Reduced graphene oxide-functionalized FeOOH for signal-on photoelectrochemical sensing of prostate-specific antigen with bioresponsive controlled release system, Biosens. Bioelectron. 98 (2017) 15–21.
[43] Y. Chen, H. Xia, W. Zhang, W. Zheng, X. Feng, J. Jiang, Template synthesis of porous hierarchical Cu_2ZnSnS_4 nanostructures for photoelectrochemical water splitting, Int. J. Hydrogen Energy 46 (3) (2021) 2862–2870.